

Emergence of insulating ferrimagnetism and perpendicular magnetic anisotropy in 3d-5d perovskite oxide composite films for insulator spintronics

Zeliang Ren^{1,2,3†}, Bin Lao^{2,3†}, Xuan Zheng^{2,3,4}, Lei Liao⁵, Zengxing Lu^{2,3}, Sheng Li^{2,3}, Yongjie Yang^{2,3}, Bingshan Cao^{1,2,3}, Lijie Wen^{2,3,6}, Kenan Zhao^{2,3}, Lifen Wang⁵, Xuedong Bai⁵, Xianfeng Hao⁶, Zhaoliang Liao^{7*}, Zhiming Wang^{2,3,8*} and Run-Wei Li^{2,3,8}

¹Nano Science and Technology Institute, University of Science and Technology of China, Hefei 230026, Anhui, China

²CAS Key Laboratory of Magnetic Materials and Devices, Ningbo Institute of Materials Technology and Engineering, Chinese Academy of Sciences, Ningbo 315201, China

³Zhejiang Province Key Laboratory of Magnetic Materials and Application Technology, Ningbo Institute of Materials Technology and Engineering, Chinese Academy of Sciences, Ningbo 315201, China

⁴New Materials Institute, University of Nottingham Ningbo China, Ningbo 315100, China

⁵Beijing National Laboratory for Condensed Matter Physics, Institute of Physics, Chinese Academy of Sciences, Beijing 100190, China

⁶Key Laboratory of Applied Chemistry, College of Environmental and Chemical Engineering, Yanshan University, Qinhuangdao 066004, China

⁷National Synchrotron Radiation Laboratory, University of Science and Technology of China, Hefei 230026, Anhui, China

⁸Center of Materials Science and Optoelectronics Engineering, University of Chinese Academy of Sciences, Beijing 100049, China

Abstract: Magnetic insulators with strong perpendicular magnetic anisotropy (PMA) play a key role in exploring pure spin current phenomena and developing ultralow-dissipation spintronic devices, thereby it is highly desirable to develop new material platforms. Here we report epitaxial growth of $\text{La}_{2/3}\text{Sr}_{1/3}\text{MnO}_3$ (LSMO)- SrIrO_3 (SIO) composite oxide films (LSMIO) with different crystalline orientations fabricated by sequential two-target ablation process using pulsed laser deposition. The LSMIO films exhibit high crystalline quality with homogeneous mixture of LSMO and SIO at atomic level. Ferrimagnetic and insulating transport characteristics are observed, with the temperature-dependent electric resistivity well fitted by Mott variable-range-hopping model. Moreover, the LSMIO films show strong PMA. Through further constructing all perovskite oxide heterostructures of the ferrimagnetic insulator LSMIO and a strong spin-orbital coupled SIO layer, pronounced spin Hall magnetoresistance (SMR) and spin Hall-like anomalous Hall effect (SH-AHE) were observed. These results illustrate the potential application of the ferrimagnetic insulator LSMIO in developing all-oxide ultralow-dissipation spintronic devices.

Keywords: Perovskite oxide, magnetic insulator, perpendicular magnetic anisotropy, spin hall magnetoresistance, spintronics

INTRODUCTION

In order to satisfy the ever-increasing demanding of information storage capacity and processing speed, reducing the energy consumption of electronic devices becomes more and more important in the microelectronics industry. In contrast to conventional microelectronics relying only the charge of electrons, spintronics use the additional spin of electrons to encode, store, process and transmit data, which is very promising to bring new capabilities to microelectronic devices¹⁻³. Especially, spintronics based on ferromagnetic/ferrimagnetic magnetic insulators (FMI) has attracted tremendous attention for developing ultralow-dissipation devices. The local magnetic moments in FMI act as ideal media for pure spin angular momentum propagating while the thermal consumptions such as Joule heating can be efficiently avoided by suppressing the moving of electrons⁴⁻⁶. Additionally, magnets with perpendicular magnetic anisotropy (PMA), where the magnetic easy axis preferentially points toward normal to the surface, is essentially required to reduce the devices size while maintaining high thermal stability⁷⁻¹¹. Combination of FMI and PMA further provides exciting functionalities for lowering current threshold and enhancing mobility of domain wall displacement, as well as achieving long decay length during spin-wave propagation¹². Therefore, the development of FMI with PMA is much meaningful for the development of high-performance spintronic devices.

Magnetic insulators are frequently found in transition metal oxides with various crystal structures, such as rocksalt, perovskite, spinel, and garnet. Among them, perovskite ABO_3 oxides are particularly promising candidates to achieve high-quality all-oxides spintronic devices because of their versatile functionalities, including spin source generator, spin current detector and so on^{13, 14}. However, magnetic insulators in perovskites often favor antiferromagnetism instead of ferromagnetic ordering, due to the super-exchange interaction between neighboring magnetic ions according to Goodenough-Kanamori-Anderson rules¹⁵. Moreover, FMI with strong PMA in perovskite oxides are rarely reported. Manganite $La_{1-x}Sr_xMnO_3$ (LSMO), as an archetypal colossal magnetoresistance materials, have been widely studied on account of its rich phase diagrams where multiple electric and magnetic properties are present^{16, 17}. Previous studies had demonstrated that PMA can be obtained in LSMO films and heterostructures through engineering the lattice and orbital degrees of freedom¹⁸⁻²⁰. Recently, strong PMA can be triggered in LSMO when interfacing with strong spin-orbital coupled $SrIrO_3$ (SIO)^{21, 22}. However, the LSMO maintained metallic in most cases, unless large strain was imposed²³⁻²⁵. Through A- or/and B-site cation substitutions in ABO_3 the spin polarization of band structure can be directly controlled,

leading to modified exchange interactions and associated magnetic and electrical ground states²⁶. Thanks to the advances in epitaxial synthesis techniques, composite films have emerged as powerful platforms for realizing FMI and strong PMA in LSMO-based perovskite oxides since deliberating control of specific atoms can be realized²⁷. Given these reasons, emergent FMI with strong PMA can be obtained via engineering cation substitution in LSMO and SIO, which enables to explore pure spin current phenomena in all-oxide heterostructures.

In this letter, we reported a facile method to fabricate LSMO-SIO (LSMIO) composite oxide films that are mixed homogeneously at atomic level. The LSMIO films are FMI with PMA, whose temperature-dependent resistivity was fitted well by Mott variable-range-hopping model. By further constructing heterostructures of FMI LSMIO and strong spin-orbital coupled SIO layers, we explored pure spin current phenomena and observed pronounced spin Hall magnetoresistance (SMR) and spin Hall-like anomalous Hall effect (SH-AHE). These results demonstrate that FMI LSMIO is promising for exploring insulator spintronics in all oxides heterostructures and developing low-dissipation spintronic devices.

RESULTS AND DISCUSSION

Figure 1(a) shows the schematics of sequential two-target deposition process of LSMIO films using pulsed laser deposition (PLD). During the growth, the LSMO and SIO targets were rotated repeatedly and periodically. In each repeat, sub-monolayer 0.3 unit cell (u.c.) LSMO and 0.2 u.c. SIO were deposited, ensuring homogeneous mixture of two ceramic targets at the atomic scale. The LSMIO films have a nominal stoichiometry of $\text{La}_{0.4}\text{Sr}_{0.6}\text{Mn}_{0.6}\text{Ir}_{0.4}\text{O}_3$. The crystalline orientation of LSMIO films can be controlled by changing substrate orientation. The crystalline structures were characterized by X-Ray diffraction (XRD) 2θ - θ scans as shown in Fig. 1(b). The peaks of LSMIO films are labeled and are located on the left side of SrTiO_3 (STO) substrates closely. This result indicates that the films are slightly compressed (<0.1%) and of high-quality single crystal without impurity phases. To further characterize the interface quality and structural homogeneity, scanning transmission electron microscopy (STEM) measurements on the (001)-oriented LSMIO films, as shown in Figs. 1(c)-1(h), were performed. The sharp contrast across the LSMIO and STO substrates in Fig. 1(c), supplemented by a high-angle annular dark-field (HAADF) STEM image of the LSMIO films in Fig. 1(d), indicates high crystalline quality of the films. Figures 1(e)-1(h) show the corresponding energy dispersive X-ray spectroscopy (EDS) mappings of La, Sr, Mn and Ir elements. All measured elements are distributed homogeneously at atomic level in the composite films without observable clustering regions.

To investigate the magnetic properties of LSMIO composite films, we measured magnetic hysteresis (M - H) loops and temperature-dependent magnetization (M - T) curves. Figures 2(a)-2(c) display the M - H loops observed with the magnetic field applied parallel ($H \perp c$) and perpendicular ($H // c$) to the film plane for differently oriented LSMIO composite films. The coercive field is found to be 0.67 T, which is much larger than that of soft ferromagnetic LSMO films. On the other hand, we note that the saturation moments are determined to be around $2.4 \mu_B/\text{u.c.}$, which are considerably smaller than that in LSMO films²⁸. The reduction of the saturation moments can be explained by the antiferromagnetic coupling in the Mn-O-Ir bonds as evidenced from the first-principle calculations shown below, which leads to the ferrimagnetic ground state in LSMIO composite films. Figure 2(d) show the corresponding magnetization M as a function of temperature. The Curie temperature (T_C) becomes lower for all the LSMIO films as compared to pure LSMO bulk material. Intriguingly, by comparing the magnetic hysteresis loops measured under field parallel and perpendicular to films respectively, it is found that all easy magnetization axes are perpendicular to the film plane for all LSMIO films regardless of the crystal orientation while the magnetic anisotropy energy are 1.21×10^6 , 1.55×10^6 and 1.56×10^6 erg/cm³ respectively, which are comparable with the PMA reported in LSMO/SIO heterostructures²². Therefore, it is feasible to obtain perovskite FMI with strong PMA in LSMIO composite films. Considering the negligible compressive strain imposed by the SrTiO₃ substrates, the observed strong PMA is not due to magneto-elastic anisotropy as been observed previously in LSMO films or heterostructures when under large compressive strain^{24, 25}. The strong PMA is due to the magnetic crystalline anisotropy originated from strong spin-orbital coupling and Mn-O-Ir bonding^{21, 22, 29}

To further understand the electrical properties of LSMIO composite films, we have performed the temperature-dependent electric resistivity measurements. As shown in Fig. 2(e), the resistivity increases monotonically as the temperature decreases, indicating that all the LSMIO composite films are insulators. This is in sharp contrast to individual LSMO and SIO films which are metallic and semi-metallic in their bulk counterparts, respectively. To illustrate the origin of the emergent FMI state, we have fitted the resistivity data with thermal activation, Efros–Shklovskii variable-range-hopping (ES-VRH) and Mott variable-range-hopping (Mott-VRH) models, as shown in Figs. S3 (b)-(c) respectively. Figure 2(f) depicts the linear fitting curves using Mott-VRH model, which agrees well to the measured resistivity. Here, the Mott-VRH model is expressed as the following equation:

$$\rho(T) = \rho_{(0)} \exp\left(T_M/T\right)^{(1/d+1)}$$

Where ρ_0 is resistance coefficient, T_M is characteristic temperature and the exponent d depends on the VRH mechanism. For the Mott VRH conduction, the exponent d is dimension dependent and has a value of $d = 3$ in a three-dimensional system³⁰⁻³². From the fitted characteristic temperature T_M , we can infer the Mott hopping energy (E_M) as:

$$E_M = \frac{1}{4} k_B T \left(T_M/T\right)^{1/4}$$

The fitted hopping energy for (001)-, (110)- and (111)-oriented LSMIO composite films are determined to be 72.2, 93.7 and 117.2 meV at room temperature (300 K), respectively. The Mott-VRH model describes that the localized electron at the Fermi level moves to another localized state in an optimum hoping distance which is determined by the tradeoff between the lowest energy differences and the shortest hopping distances in a disordered system³³. Given that the Mn-O-Ir bonds are dominated in the LSMIO composite oxide films, the Mott-VRH behavior suggests that the carriers hopping through the Mn-O-Ir bonds are suppressed and form localized states. This situation is in sharp contrast with metallic Mn-O-Mn bonds in LSMO films, where the electrons can itinerantly hop between neighboring Mn³⁺ and Mn⁴⁺ ions through the double-exchange mechanism^{17, 34}.

To gain further insight into the electronic and magnetic properties of LSMIO nanocomposite films, we have performed first-principles calculations based on the double perovskite model LaSrMnIrO₆ (Fig. 3(a)). From the total energy results of the distinct magnetic solutions (schematically shown in Fig. 4S and Tab. S2 in Supplementary Materials), we found that the ferrimagnetic, uncompensated antiferromagnetic alignment, due to the unequal magnetic moments on Mn and Ir sites, is the most stable state for LSMIO, affirming the experimental observations. Moreover, the GGA+U schemes prefer quite stable magnetic solution with magnetic moments of Mn ($\sim 4.3 \mu_B$) and Ir ($\sim -0.9 \mu_B$) ions, accompanied by considerable induced magnetic moments ($\sim -0.1 \mu_B$) for all the surrounding O²⁻ anions as demonstrated in Fig. 3(b). Unexpected, the magnetic moment at Mn sites is slightly larger than the ideal spin-only $4 \mu_B$ for Mn³⁺ cations, suggesting the special magnetic coupling mechanism behind. Figure 3(c) shows that the ferrimagnetic ground state is insulating with a band gap of 0.2 eV, which agrees well with the experimental temperature-dependent electric

resistivity data. The antiferromagnetic coupling and unexpected large magnetic moment on Mn³⁺ site can be interpreted in the framework of superexchange interactions through the virtual hopping bridged by O 2*p* spin-up electrons, as illustrated in Fig. 3(d), which is derived from the partial density of states and spin density plots. We can see that the virtual hopping from Ir *t*_{2*g*}[↑] to the empty Mn *e*_{*g*}[↑] via the bridged O 2*p*[↑] states accounts for the antiferromagnetic coupling and the abnormal large computed Mn³⁺ magnetic moment as well as the exclusively negative sign of the induced O²⁻ magnetic moments.

Finally, to explore the application of FMI LSMIO in pure spin current phenomenon, we fabricated a LSMIO/SIO heterostructure and performed temperature-dependent magnetoresistance measurements. Figures 4(a)-4(b) show schematic structure of Hall bar devices and measurement geometry. As illustrated in Fig. 4(a), the heterostructure consists of the FMI LSMIO and a strong spin-orbital coupled SIO layer. The SIO layer can efficiently convert the charge current into spin current^{35, 36}, so a pronounced SMR can be expected due to the asymmetry between absorption and reflection of the spin current at the LSMIO/SIO interface. Figure 4(c) depicts the angle dependent magnetoresistance measurements where external field rotates in the y-z plane around angle β . It is necessary to distinguish the difference between SMR and anisotropic magnetoresistance (AMR). SMR signal is known to be described as:

$$\rho_{xx} = \rho_0 - \Delta\rho m_y^2$$

while AMR signal is described as:

$$\rho_{xx} = \rho_0 - \Delta\rho m_x^2$$

In these two formulas, the ρ_0 is constant resistivity offset, $\Delta\rho$ is amplitude of the resistivity change as a function of the magnetization orientation and m_i ($i = x, y$) is the projections of the magnetization orientation unit vector along x and y axis in the coordinate system³⁷⁻³⁹. Note that $\rho_{xx} = v_{xx}wt/J_q l$ and $\rho_{xy} = v_{xy}t/J_q$, where w is channel width ($w = 10$ μm), the l is the length of the separated voltage contacts ($l = 50$ μm) and the t is the thickness of SIO layer ($t = 5$ nm). During the measurement, the external field was fixed to 4 T which is much larger than the coercive field of LSMIO (0.67 T) in order to obtain collinear magnetization. Figure 4(c) shows that the resistivity data exhibit the $\cos^2\beta$ dependence. This is in consistent with the SMR signal since m_y has $\cos\beta$ dependence, while AMR keep constant in angle β dependent measurements

since m_x equals to 0. These measurements demonstrate that the SMR can be detected in all perovskite oxide heterostructures.

Figure 4(d) shows the Hall resistance measurements with the magnetic field applied perpendicular to the sample and varied from -4 T to 4 T. By subtracting a linear contribution from ordinary Hall effect, a clear hysteresis loop curve is visible, which resembles the AHE. Figure 4(e) shows the temperature-dependent Hall resistance after subtracting a linear term. The coercive field inferred from the Hall hysteresis loop is about 0.67 T at 10 K, which is similar as that of LSMIO films measured by SQUID shown in Fig. 2(a). Moreover, the coercive field decreases as a function of temperature and becomes invisible at above 120 K. These results demonstrate that the evolution of AHE with temperature resembles that of the magnetization versus temperature curve as shown in Fig. 2(d), indicating that the observed AHE is closely related to the PMA of LSMIO composite films. We note that interfacial magnetism and AHE has been intensively studied in LSMO/SIO superlattices and heterostructures^{21, 40-46}. Our observed AHE is quite different from that the AHE reported in ref. 41, where a large AHE is originated from SIO layers due to magnetic proximity effect. Our AHE stems from the reflection of the spin current at the interface where an out-of-plane component (m_z) of the LSMIO magnetization rotates the spin orientation of the spin current and generates a transverse voltage via the inverse spin Hall effect (ISHE). Such AHE is termed as SH-AHE^{47, 48}. Therefore, both SMR and SH-AHE indicate occurrence of the spin transfer at the interface of the conductor and ferrimagnetic insulator. The spin current can be injected into insulators which gives a possibility of transmitting spin information through an insulator. Such behavior would have an advantage of ultralow power dissipation due to absence of Joule heating.

CONCLUSION

In conclusion, we have synthesized LSMIO composite oxide films with different crystalline orientations by sequential two-target deposition process. The LSMIO composite films exhibit high crystalline quality with homogeneous mixture of LSMO and SIO at atomic level. The electric and magnetic measurements, complemented by first-principle calculations, indicate that the LSMIO composite films are FMI with strong PMA. The temperature-dependent electric resistivity is well described by Mott-VRH model. Furthermore, through fabricating heterostructures of the FMI LSMIO and a strong spin-orbital coupled SIO layer, we observed pronounced SMR and SH-AHE. These results illustrate the potential application of LSMIO in developing all-oxide ultralow-dissipation spintronic devices. Given the scarcity of perovskite FMI with strong PMA, our result provides a promising real material candidate to boost the development of insulating spintronics devices.

EXPRIMENTAL SECTION

Sample preparation: LSMIO composite films were synthesized by PLD, equipped with KrF ($\lambda=248$ nm) excimer laser and high reflection high energy electron diffraction (RHEED). Prior to the film deposition, (001)-, (110)- and (111)-oriented STO substrates were etched by NH_4F -buffered hydrofluoric acid followed by annealing at 1100 °C for 90 minutes. During films deposition, the temperature of substrates, oxygen partial pressure and laser fluence were set to 700 °C, 0.1 mbar and 1.5 J/cm² at the frequency of 2 Hz, respectively. The film growth was monitored by RHEED and the thickness was determined to be 12 nm.

Sample characterizations: The quality and structure of the films was characterized by XRD (Bruker), STEM and EDS (JEOL Grand ARM 300), respectively. The magnetic and electric properties were measured by Quantum Design Magnetic Property Measurement System (MPMS-SQUID, Quantum Design) and Physical Property Measurement System (PPMS, Quantum Design). Further investigations of spin-related SMR and AHE were performed on Hall bar devices composed of LSMIO and SIO using a home-build low-temperature and high-intensity magnetic field magneto-electric system. The LSMIO/SIO heterostructures were prepared by PLD as the same condition with LSMIO films. The as grown (001)-oriented LSMIO/SIO heterostructure was patterned into Hall bars by photolithography and Ar ion etching.

First-principle calculations: In order to describe the structure of LSMIO composite films, we constructed the canonical perovskite-type model within $2\times 2\times 2$ supercell ($\text{La}_4\text{Sr}_4\text{Mn}_4\text{Ir}_4\text{O}_{24}$, 40 atoms). The spin-polarized density functional theory (DFT) calculations are achieved with the plane wave basis set as implemented in the Vienna *ab initio* simulation package^{49, 50}. For the exchange correlation functional, the generalized gradient approximation (GGA) is used according to the Perdew-Burke-Ernzerhof scheme⁵¹, and GGA+U approaches^{52, 53} are also performed for including the static electron correlation, with the Hubbard $U = 4$ eV (2 eV) and Hund $J = 0.8$ eV (0.4 eV) for Mn $3d$ (Ir $5d$) states. A plane-wave energy cutoff of 400 eV was employed. The k -point meshes over the total Brillouin zone were sampled by $4\times 4\times 4$ and $6\times 6\times 6$ grids constructed according to the Monkhorst-Pack scheme^{54, 55} for structural relaxations and electronic calculations, respectively. We optimized the lattice vectors, volumes, as well as internal atomic with the relaxation terminated once the total energies and residual atomic forces converged to $< 1\times 10^{-5}$ eV and $< |0.01|$ eV/Å, respectively.

■ AUTHOR INFORMATION

Corresponding Author

zlia@ustc.edu.cn.

zhiming.wang@nimte.ac.cn.

Author contribution

†Z.R. and B.L. contributed equally to this work. Z.W. designed the experiments. Z.R. performed sample growth. Structure characterization, magnetic and transport measurements were performed by Z.R., B.L., X.Z., Z.L., S.L., B.C., L.W., and K.Z. L.L., L.W. and X.B. performed STEM measurements. Z.R. and B.L. performed data analysis. X.H. performed first-principle calculations and data analysis. Z.R., B.L., X.H., Z.L. and Z.W. wrote the manuscript. All authors participated in discussions and approved the submitted manuscript.

■ ACKNOWLEDGMENTS

This work was supported by the National Key Research and Development Program of China (Nos. 2017YFA0303600, 2019YFA0307800), the National Natural Science Foundation of China (Nos. 12174406, U1832102, 11874367, 51931011, 51902322), the Key Research Program of Frontier Sciences, Chinese Academy of Sciences (No. ZDBS-LY-SLH008), the Thousand Young Talents Program of China, K.C.Wong Education Foundation (GJTD-2020-11), the 3315 Program of Ningbo, the Natural Science Foundation of Zhejiang province of China (No. LR20A040001), the Beijing National Laboratory for Condensed Matter Physics.

■ REFERENCES

1. Bader, S. D.; Parkin, S. S. P., Spintronics. *Annu. Rev. Condens. Matter Phys.* **2010**, *1*, 71.
2. Shiraishi, M.; Ikoma, T., Molecular spintronics. *Physica E Low Dimens. Syst. Nanostruct.* **2011**, *43*, 1295.
3. Hirohata, A.; Yamada, K.; Nakatani, Y.; Prejbeanu, I.-L.; Diény, B.; Pirro, P.; Hillebrands, B., Review on spintronics: Principles and device applications. *J. Magn. Magn. Mater.* **2020**, *509*, 166711.
4. Bauer, G. E.; Saitoh, E.; van Wees, B. J., Spin caloritronics. *Nat. Mater.* **2012**, *11*, 391.
5. Kajiwara, Y.; Harii, K.; Takahashi, S.; Ohe, J.; Uchida, K.; Mizuguchi, M.; Umezawa, H.; Kawai, H.; Ando, K.; Takanashi, K.; Maekawa, S.; Saitoh, E., Transmission of electrical signals by spin-wave interconversion in a magnetic insulator. *Nature* **2010**, *464*, 262.
6. Gilleo, M. A., Ferromagnetic insulators: Garnets. *Handb. Magn. Mater* **1980**, *2*, 1-53.
7. Diény, B.; Chshiev, M., Perpendicular magnetic anisotropy at transition metal/oxide interfaces and applications. *Rev. Mod. Phys.* **2017**, *89*, 025008.

8. Mangin, S.; Ravelosona, D.; Katine, J. A.; Carey, M. J.; Terris, B. D.; Fullerton, E. E., Current-induced magnetization reversal in nanopillars with perpendicular anisotropy. *Nat. Mater.* **2006**, *5*, 210.
9. Ikeda, S.; Miura, K.; Yamamoto, H.; Mizunuma, K.; Gan, H. D.; Endo, M.; Kanai, S.; Hayakawa, J.; Matsukura, F.; Ohno, H., A perpendicular-anisotropy CoFeB-MgO magnetic tunnel junction. *Nat. Mater.* **2010**, *9*, 721.
10. Wang, M.; Cai, W.; Cao, K.; Zhou, J.; Wrona, J.; Peng, S.; Yang, H.; Wei, J.; Kang, W.; Zhang, Y.; Langer, J.; Ocker, B.; Fert, A.; Zhao, W., Current-induced magnetization switching in atom-thick tungsten engineered perpendicular magnetic tunnel junctions with large tunnel magnetoresistance. *Nat. Commun.* **2018**, *9*, 671.
11. Wang, M.; Cai, W.; Zhu, D.; Wang, Z.; Kan, J.; Zhao, Z.; Cao, K.; Wang, Z.; Zhang, Y.; Zhang, T.; Park, C.; Wang, J.-P.; Fert, A.; Zhao, W., Field-free switching of a perpendicular magnetic tunnel junction through the interplay of spin-orbit and spin-transfer torques. *Nat. Electron.* **2018**, *1*, 582.
12. Velez, S.; Schaab, J.; Wornle, M. S.; Muller, M.; Gradauskaite, E.; Welter, P.; Gutgsell, C.; Nistor, C.; Degen, C. L.; Trassin, M.; Fiebig, M.; Gambardella, P., High-speed domain wall racetracks in a magnetic insulator. *Nat. Commun.* **2019**, *10*, 4750.
13. Tokura, Y.; Kawasaki, M.; Nagaosa, N., Emergent functions of quantum materials. *Nat. Phys.* **2017**, *13*, 1056.
14. Bhattacharya, A.; May, S. J., Magnetic Oxide Heterostructures. *Annu. Rev. Mater. Sci.* **2014**, *44*, 65.
15. Goodenough, J., Magnetism and the Chemical Bond. J. Wiley and Sons, New York—London. *Phys. Rev.* **1963**, *117*, 1442.
16. Hemberger, J.; Krimmel, A.; Kurz, T.; Krug von Nidda, H. A.; Ivanov, V. Y.; Mukhin, A. A.; Balbashov, A. M.; Loidl, A., Structural, magnetic, and electrical properties of single-crystalline $\text{La}_{1-x}\text{Sr}_x\text{MnO}_3$ ($0.4 < x < 0.85$). *Phys. Rev. B* **2002**, *66*, 1-8.
17. Cesaria, M.; Caricato, A. P.; Maruccio, G.; Martino, M., LSMO – growing opportunities by PLD and applications in spintronics. *J. Phys. Conf. Ser.* **2011**, *292*, 012003.
18. Zhang, J.; Chen, X.; Zhang, Q.; Han, F.; Zhang, J.; Zhang, H.; Zhang, H.; Huang, H.; Qi, S.; Yan, X.; Gu, L.; Chen, Y.; Hu, F.; Yan, S.; Liu, B.; Shen, B.; Sun, J., Magnetic Anisotropy Controlled by Distinct Interfacial Lattice Distortions at the $\text{La}_{1-x}\text{Sr}_x\text{CoO}_3/\text{La}_{2/3}\text{Sr}_{1/3}\text{MnO}_3$ Interfaces. *ACS Appl. Mater. Interfaces* **2018**, *10*, 40951.
19. Zhang, J.; Zhong, Z.; Guan, X.; Shen, X.; Zhang, J.; Han, F.; Zhang, H.; Zhang, H.; Yan, X.; Zhang, Q.; Gu, L.; Hu, F.; Yu, R.; Shen, B.; Sun, J., Symmetry mismatch-driven perpendicular magnetic anisotropy for perovskite/brownmillerite heterostructures. *Nat. Commun.* **2018**, *9*, 1923.
20. Han, F.; Chen, X.; Wang, J.; Huang, X.; Zhang, J.; Song, J.; Liu, B.; Chen, Y.; Bai, X.; Hu, F., Perpendicular magnetic anisotropy induced by $\text{La}_{2/3}\text{Sr}_{1/3}\text{MnO}_3\text{-YBaCo}_2\text{O}_{5+\delta}$ interlayer coupling. *J. Phys. D: Appl. Phys.* **2021**, *54*, 185302.
21. Nichols, J.; Gao, X.; Lee, S.; Meyer, T. L.; Freeland, J. W.; Lauter, V.; Yi, D.; Liu, J.; Haskel, D.; Petrie, J. R.; Guo, E. J.; Herklotz, A.; Lee, D.; Ward, T. Z.; Eres, G.; Fitzsimmons, M. R.; Lee, H. N., Emerging magnetism and anomalous Hall effect in iridate-manganite heterostructures. *Nat. Commun.* **2016**, *7*, 12721.

22. Yi, D.; Flint, C. L.; Balakrishnan, P. P.; Mahalingam, K.; Urwin, B.; Vailionis, A.; N'Diaye, A. T.; Shafer, P.; Arenholz, E.; Choi, Y.; Stone, K. H.; Chu, J. H.; Howe, B. M.; Liu, J.; Fisher, I. R.; Suzuki, Y., Tuning Perpendicular Magnetic Anisotropy by Oxygen Octahedral Rotations in $(\text{La}_{1-x}\text{Sr}_x\text{MnO}_3)/(\text{SrIrO}_3)$ Superlattices. *Phys. Rev. Lett.* **2017**, *119*, 077201.
23. Wang, B.; You, L.; Ren, P.; Yin, X.; Peng, Y.; Xia, B.; Wang, L.; Yu, X.; Poh, S. M.; Yang, P.; Yuan, G.; Chen, L.; Rusydi, A.; Wang, J., Oxygen-driven anisotropic transport in ultra-thin manganite films. *Nat. Commun.* **2013**, *4*, 2778.
24. Xiao, Z.; Zhang, F.; Farrukh, M. A.; Wang, R.; Zhou, G.; Quan, Z.; Xu, X., Perpendicular magnetic anisotropy in compressive strained $\text{La}_{0.67}\text{Sr}_{0.33}\text{MnO}_3$ films. *J. Mater. Sci.* **2019**, *54*, 9017.
25. Wu, Y.; Suzuki, Y.; Rüdiger, U.; Yu, J.; Kent, A. D.; Nath, T. K.; Eom, C. B., Magnetotransport and magnetic domain structure in compressively strained colossal magnetoresistance films. *Appl. Phys. Lett.* **1999**, *75*, 2295.
26. Sun, L.; Zhang, J.; Chen, Y. B.; Zhang, S.-T.; Hong, B.; Zhao, J.; Luo, Z.; Chen, Y.-F., The significant and temperature-insensitive magnetoresistance observed in Co-doped $(\text{La}_{0.7}\text{Sr}_{0.3})\text{MnO}_3$ thin films. *AIP Adv.* **2019**, *9*, 015327.
27. Huon, A.; Yoon, S.; Fitzsimmons, M. R.; Charlton, T. R.; Ok, J. M.; Cruz, C. d.; Lee, H. N., Effects of Sn substitution in SrRuO_3 epitaxial films. *Appl. Phys. Lett.* **2021**, *119*, 112404.
28. Feng, Y.; Jin, K. J.; Gu, L.; He, X.; Ge, C.; Zhang, Q. H.; He, M.; Guo, Q. L.; Wan, Q.; He, M.; Lu, H. B.; Yang, G., Insulating phase at low temperature in ultrathin $\text{La}_{0.8}\text{Sr}_{0.2}\text{MnO}_3$ films. *Sci. Rep.* **2016**, *6*, 22382.
29. Lu, Z.; Liu, J.; Wen, L.; Feng, J.; Kong, S.; Zheng, X.; Li, S.; Jiang, P.; Zhong, Z.; Zhu, J.; Hao, X.; Wang, Z.; Li, R.-W., Lateral Modulation of Magnetic Anisotropy in Tricolor 3d-5d Oxide Superlattices. *ACS Appl. Electron. Mater.* **2021**, *3*, 4210.
30. Liu, X.; Yang, Y.; Zhang, Q.; Yan, D.; Lu, J.; Chen, R.; Shi, Y.; Xiong, C.; Wang, F.; Gu, L.; Zhang, J., Mott gap engineering in $\text{Sr}_2\text{IrO}_4/\text{SrTiO}_3$ superlattices. *Sci. China Mater.* **2020**, *63*, 1855.
31. Mott, N., Review article: The mobility edge since 1967. *J. phys., C, Solid state phys.* **1987**, *20*, 3075.
32. Chaurasia, R.; Asokan, K.; Kumar, K.; Pramanik, A. K., Low-temperature ferromagnetism in perovskite SrIrO_3 films. *Phys. Rev. B* **2021**, *103*, 1-11.
33. Xue, J.; Huang, S.; Wang, J.-Y.; Xu, H. Q., Mott variable-range hopping transport in a MoS_2 nanoflake. *RSC Adv.* **2019**, *9*, 17885.
34. Lu, Z.; Liu, J.; Feng, J.; Zheng, X.; Yang, L.-h.; Ge, C.; Jin, K.-j.; Wang, Z.; Li, R.-W., Synthesis of single-crystal $\text{La}_{0.67}\text{Sr}_{0.33}\text{MnO}_3$ freestanding films with different crystal-orientation. *APL Mater.* **2020**, *8*, 0-6.
35. Nan, T.; Anderson, T. J.; Gibbons, J.; Hwang, K.; Campbell, N.; Zhou, H.; Dong, Y. Q.; Kim, G. Y.; Shao, D. F.; Paudel, T. R.; Reynolds, N.; Wang, X. J.; Sun, N. X.; Tsymbal, E. Y.; Choi, S. Y.; Ryzhowski, M. S.; Kim, Y. B.; Ralph, D. C.; Eom, C. B., Anisotropic spin-orbit torque generation in epitaxial SrIrO_3 by symmetry design. *Proc. Natl. Acad. Sci. U.S.A.* **2019**, *116*, 16186.
36. Everhardt, A. S.; De, M.; Huang, X.; Sayed, S.; Gosavi, T. A.; Tang, Y.; Lin, C.-C.; Manipatruni, S.; Young, I. A.; Datta, S.; Wang, J.-P.; Ramesh, R., Tunable charge to spin conversion in strontium iridate thin films. *Phys. Rev. Mater.* **2019**, *3*, 1-7.
37. Chen, Y.-T.; Takahashi, S.; Nakayama, H.; Althammer, M.; Goennenwein, S. T. B.; Saitoh, E.; Bauer, G. E. W., Theory of spin Hall magnetoresistance. *Phys. Rev. B* **2013**, *87*, 144411.

38. Nakayama, H.; Althammer, M.; Chen, Y. T.; Uchida, K.; Kajiwara, Y.; Kikuchi, D.; Ohtani, T.; Geprags, S.; Opel, M.; Takahashi, S.; Gross, R.; Bauer, G. E.; Goennenwein, S. T.; Saitoh, E., Spin Hall magnetoresistance induced by a nonequilibrium proximity effect. *Phys. Rev. Lett.* **2013**, *110*, 206601.
39. Althammer, M.; Meyer, S.; Nakayama, H.; Schreier, M.; Altmannshofer, S.; Weiler, M.; Huebl, H.; Geprags, S.; Opel, M.; Gross, R.; Meier, D.; Klewe, C.; Kuschel, T.; Schmalhorst, J.-M.; Reiss, G.; Shen, L.; Gupta, A.; Chen, Y.-T.; Bauer, G. E. W.; Saitoh, E.; Goennenwein, S. T. B., Quantitative study of the spin Hall magnetoresistance in ferromagnetic insulator/normal metal hybrids. *Phys. Rev. B* **2013**, *87*, 1-15.
40. Skoropata, E.; Nichols, J.; Ok, J. M.; Chopdekar, R. V.; Choi, E. S.; Rastogi, A.; Gao, C. S. X.; Yoon, S.; Farmer, T.; Desautels, R. D.; Choi, Y.; Haskel, D.; Freeland, J. W.; Okamoto, S.; Brahlek, M.; Lee, H. N., Interfacial tuning of chiral magnetic interactions. *Sci. Adv.* **2020**, *6*, 3902.
41. Yoo, M. W.; Tornos, J.; Sander, A.; Lin, L. F.; Mohanta, N.; Peralta, A.; Sanchez-Manzano, D.; Gallego, F.; Haskel, D.; Freeland, J. W.; Keavney, D. J.; Choi, Y.; Stremper, J.; Wang, X.; Cabero, M.; Vasili, H. B.; Valvidares, M.; Sanchez-Santolino, G.; Gonzalez-Calbet, J. M.; Rivera, A.; Leon, C.; Rosenkranz, S.; Bibes, M.; Barthelemy, A.; Anane, A.; Dagotto, E.; Okamoto, S.; Te Velthuis, S. G. E.; Santamaria, J.; Villegas, J. E., Large intrinsic anomalous Hall effect in SrIrO₃ induced by magnetic proximity effect. *Nat. Commun.* **2021**, *12*, 3283.
42. Yi, D.; Liu, J.; Hsu, S. L.; Zhang, L.; Choi, Y.; Kim, J. W.; Chen, Z.; Clarkson, J. D.; Serrao, C. R.; Arenholz, E.; Ryan, P. J.; Xu, H.; Birgeneau, R. J.; Ramesh, R., Atomic-scale control of magnetic anisotropy via novel spin-orbit coupling effect in La_{2/3}Sr_{1/3}MnO₃/SrIrO₃ superlattices. *Proc. Natl. Acad. Sci. U.S.A.* **2016**, *113*, 6397.
43. Ronetti, F.; Plekhanov, K.; Loss, D.; Klinovaja, J., Magnetically confined bound states in Rashba systems. *Phys. Rev. Research* **2020**, *2*, 022052.
44. Bhowal, S.; Satpathy, S., Electronic structure and anomalous Hall effect in the ferromagnetic 3d-5d superlattice SrMnO₃/SrIrO₃. *Phys. Rev. B* **2019**, *99*, 245145.
45. Suraj, T. S.; Omar, G. J.; Jani, H.; Juvaid, M. M.; Hooda, S.; Chaudhuri, A.; Rusydi, A.; Sethupathi, K.; Venkatesan, T.; Ariando, A.; Rao, M. S. R., Tunable and enhanced Rashba spin-orbit coupling in iridate-manganite heterostructures. *Phys. Rev. B* **2020**, *102*, 125145.
46. Ovsyannikov, G. A.; Shaikhulov, T. A.; Stankevich, K. L.; Khaydukov, Y.; Andreev, N. V., Magnetism at an iridate/manganite interface: Influence of strong spin-orbit interaction. *Phys. Rev. B* **2020**, *102*, 144401.
47. Meyer, S.; Schlitz, R.; Geprags, S.; Opel, M.; Huebl, H.; Gross, R.; Goennenwein, S. T. B., Anomalous Hall effect in YIG|Pt bilayers. *Appl. Phys. Lett.* **2015**, *106*, 132402.
48. Amamou, W.; Pinchuk, I. V.; Trout, A. H.; Williams, R. E. A.; Antolin, N.; Goad, A.; O'Hara, D. J.; Ahmed, A. S.; Windl, W.; McComb, D. W.; Kawakami, R. K., Magnetic proximity effect in Pt/CoFe₂O₄ bilayers. *Phys. Rev. Mater.* **2018**, *2*, 1-5.
49. G. Kress, J. F., Efficiency of ab-initio total energy calculations for metals and semiconductors using a plane-wave basis set. *Comput. Mater. Sci.* **1996**, *6*, 15.
50. Kresse, G.; Hafner, J., Ab initio molecular dynamics for liquid metals. *Phys. Rev. B Condens. Matter* **1993**, *47*, 558.
51. John P. Perdew, K. B., Matthias Ernzerhof, Generalized Gradient Approximation Made Simple. *Phys. Rev. Lett.* **1996**, *77*, 3865.

52. Anisimov, V. I.; Aryasetiawan, F.; Lichtenstein, A. I., First-principles calculations of the electronic structure and spectra of strongly correlated systems: theLDA+Umethod. *J. Phys. Condens. Matter* **1997**, *9*, 767.
53. Anisimov, V. V.; Zaanen, J.; Andersen, O. K., Band theory and Mott insulators: Hubbard U instead of Stoner I. *Phys. Rev., B Condens. Matter* **1991**, *44* , 943.
54. John P. Perdew, K. B., Yue Wang, Generalized gradient approximation for the exchange-correlation hole of a many-electron system. *Phys. Rev. B* **1996**, *54*.
55. Elsasser, C.; Fahnle, M.; Chan, C. T.; Ho, K. M., Density-functional energies and forces with Gaussian-broadened fractional occupations. *Phys. Rev., B Condens. Matter* **1994**, *49*, 13975.

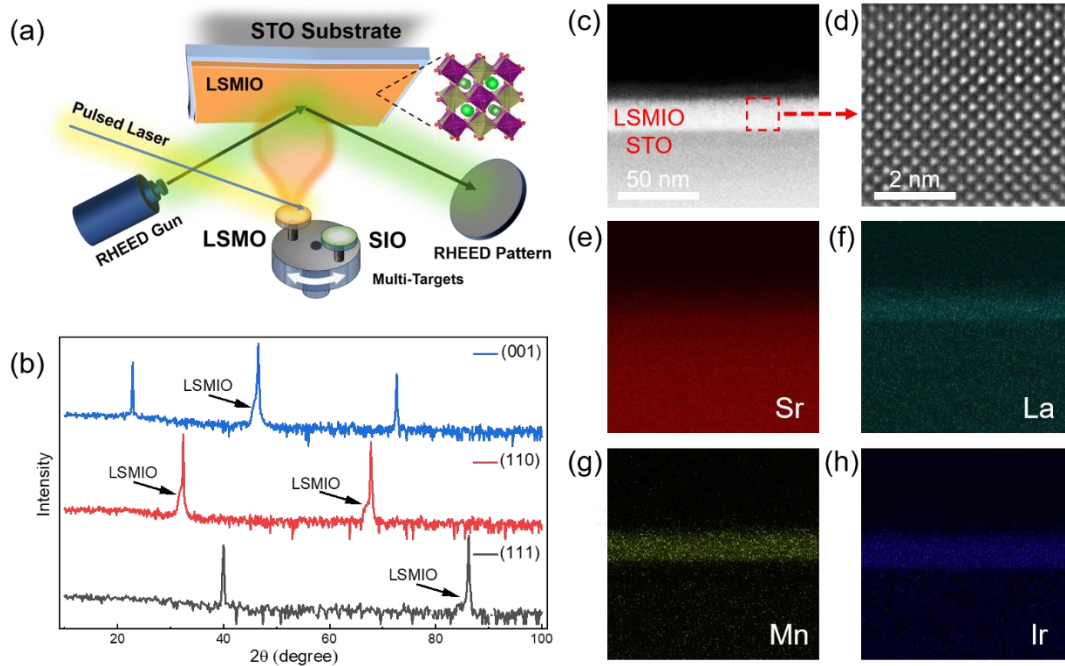


Figure 1. (a) Schematic illustration of sequential two-target deposition process of LSMIO films. (b) XRD 2θ - θ scans of LSMIO films with (001), (110) and (111) crystalline orientations. (c) HAADF-STEM images of the (001)-oriented LSMIO/STO. The high-magnification image in (b) correspond to the single crystalline LSMIO films. (e)-(h) The corresponding EDS mappings of La, Mn, Ir and Sr elements, respectively, confirming cation distribution homogeneously at atomic level.

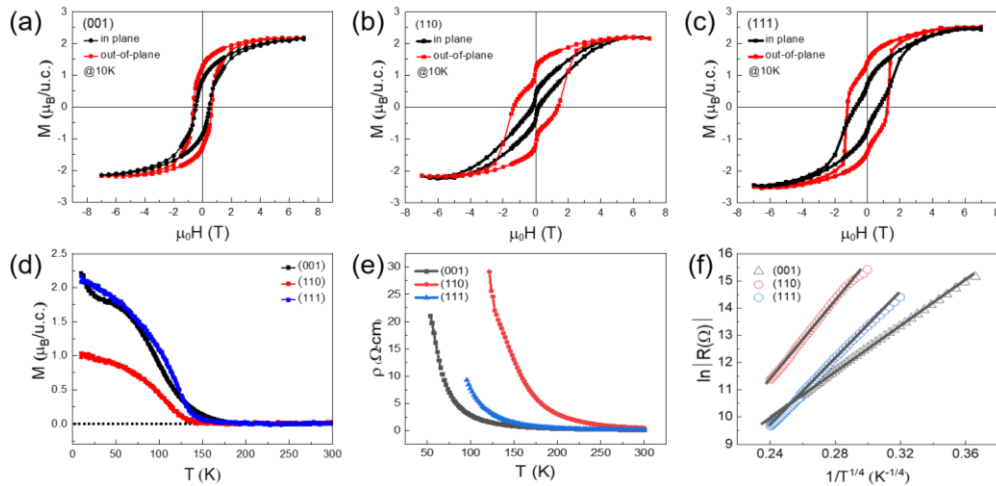


Figure 2. (a)-(c) Magnetic hysteresis loops measured with the magnetic field H applied along in-plane (black) and out-of-plane (red) for LSMIO composite films with different crystalline orientations. (d)-(e) The corresponding magnetization M and electric resistivity as a function of temperature T for different oriented LSMIO composite films. (f) The resistivity data are plotted with $\ln R \sim 1/T^{1/(d+1)}$ ($d = 3$) to fit with the three-dimensional Mott-VRH model.

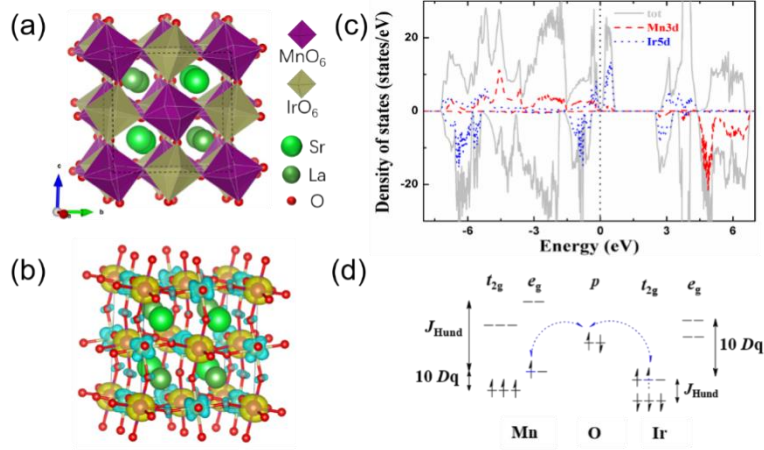


Figure 3. (a) Double perovskite structure of LaSrMnIrO_6 , in which the Mn atoms (medium purple spheres) and the Ir atoms (medium brown ones) are surrounded by O_6 octahedron denoted by small red spheres, while the light (dark) green spheres are Sr (La) atoms. (b) Isosurfaces of the spin density ($0.02 \text{ e}/\text{\AA}^2$) for double double perovskite LaSrMnIrO_6 , within the ferrimagnetic magnetic ground state. Yellow and cyan color denote spin up and spin down, respectively. (c) Total and partial density of states of Mn-3d and Ir-5d orbitals for LaSrMnIrO_6 . Majority and minority spin are presented in the top and bottom channels, respectively. (d) Schematic representation of the superexchange interaction through the Mn-O-Ir bonds. The virtual electron hopping results into the antiferromagnetic coupling between Mn-O-Ir bonds.

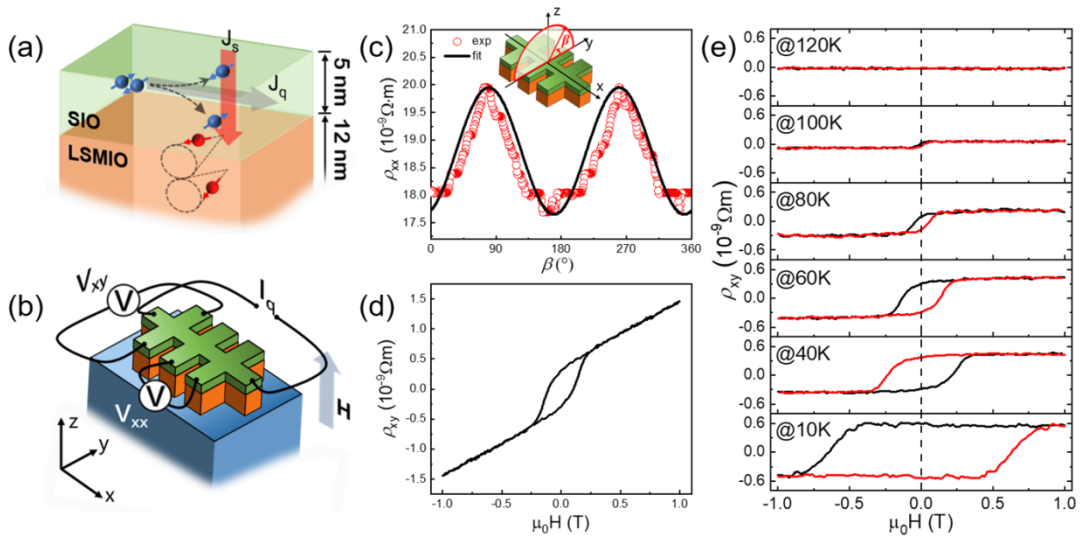


Figure 4. (a) Illustration of the SMR in LSMIO/SIO heterostructure. (b) Schematic sample structure and measurement geometry. (c) The angle dependent SMR signal. The inset shows the measurement geometry with external field rotating in the y - z plane around angle β . (d) Transverse Hall resistivity ρ_{xy} measured with the magnetic field applied perpendicular to the film plane; (e) Temperature dependent AHE sign

Supplemental Information

1. Structural characterization of LSMIO and LSMIO/SIO heterostructure.

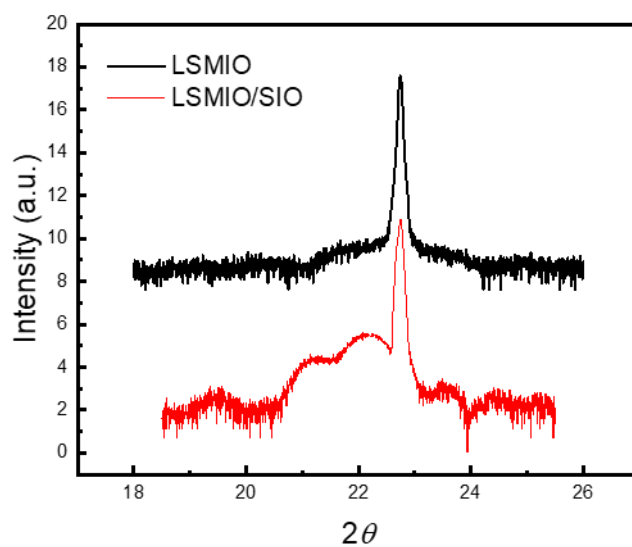


Figure S1. XRD scans of LSMIO and LSMIO/SIO heterostructure.

As shown in Fig. S1, the peak of SIO and LSMIO can be seen clearly in LSMIO/SIO heterostructure while there is only one peak of LMSIO in single LSMIO layer which means there is only one single crystal of LSMO-SIO composite films.

2. Structural characterization of LSMIO composite films by STEM

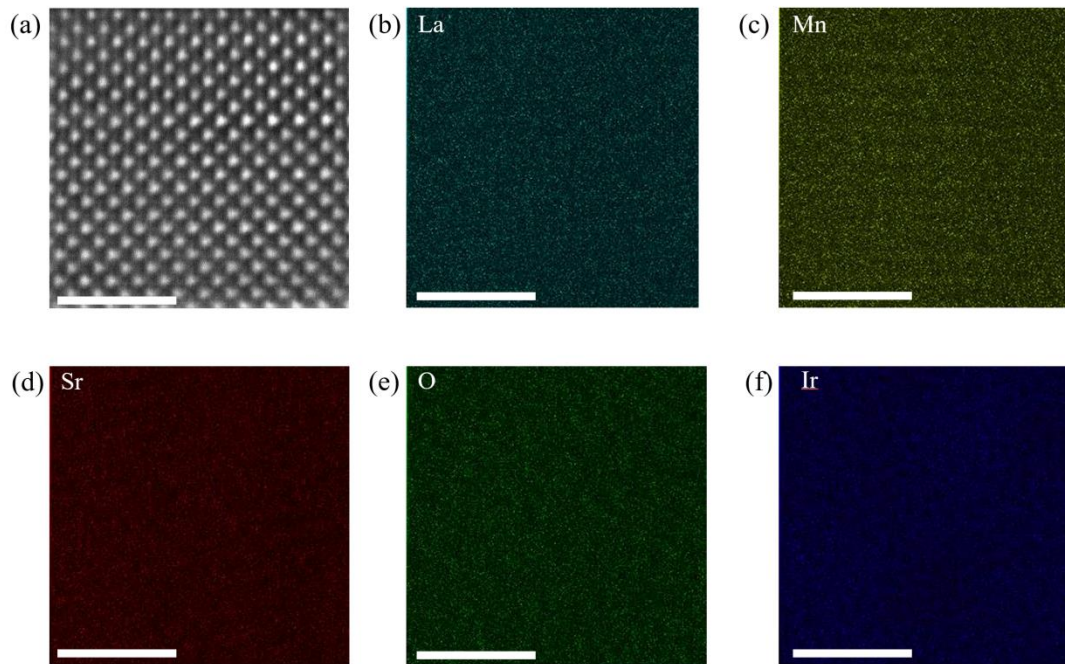


Figure S2 (a) High-resolution HAADF-STEM image of the LSMIO films (b-f) EDS maps of La, Mn, Sr, O and Ir for LSMIO films, Scale bar:2nm.

We can see the homogeneously mixture of atoms in LSMIO films in Figs S2(b)-(f).

3. The fittings of measured resistivity of LSMIO.

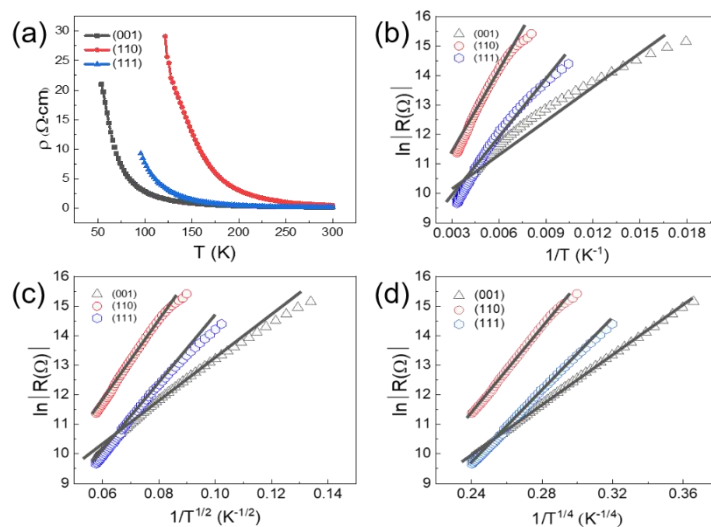


Figure S3. (a) Temperature-dependent electric resistivity of LSMIO composite films with different crystalline orientations. (b)-(d) The resistivity data are plotted with $\ln R \sim 1/T^{1/(d+1)}$ ($d = 0, 1, 3$) to fitted with the thermal activation, Efros–Shklovskii-VRH and Mott-VRH model respectively.

In this picture, we plot the resistivity with different physical model with thermal activation ($d=0$), Efros–Shklovskii-VRH ($d=1$) and 3-dimensional Mott-VRH ($d=3$). However, the nonlinearity of the curves in the Fig. S3(b)-(c) indicate that the thermal activation model cannot well fit the resistivities of LSMIO while only the Mott-VRH fits well to the measured resistivity which can be seen in Fig. S3(d).

4. DFT calculations.

In order to describe the structure of LSMIO composite films, we constructed the canonical perovskite-type model within $2 \times 2 \times 2$ supercell ($\text{La}_4\text{Sr}_4\text{Mn}_4\text{Ir}_4\text{O}_{24}$, 40 atoms), with aid of the experimental characterizations, which can be pictured as a framework consisting of alternative corners sharing MnO_6 and IrO_6 octahedra separated by $\text{La}^{3+}/\text{Sr}^{2+}$ ions, due to the quite different charge states and ionic sizes of $3d$ and $5d$ cations. Concerning the $\text{La}^{3+}/\text{Sr}^{2+}$ ions distributions, the columnar $\text{La}^{3+}/\text{Sr}^{2+}$ cation order is taken (Fig. 3(a)), as it is prevailing among the nine possible double double $\text{AA}'\text{BB}'\text{O}_6$ perovskite¹. Owing to the rotation and tilting of MnO_6 and IrO_6 octahedra, the Mn-O-Ir bond angles significantly deviate from 180° .

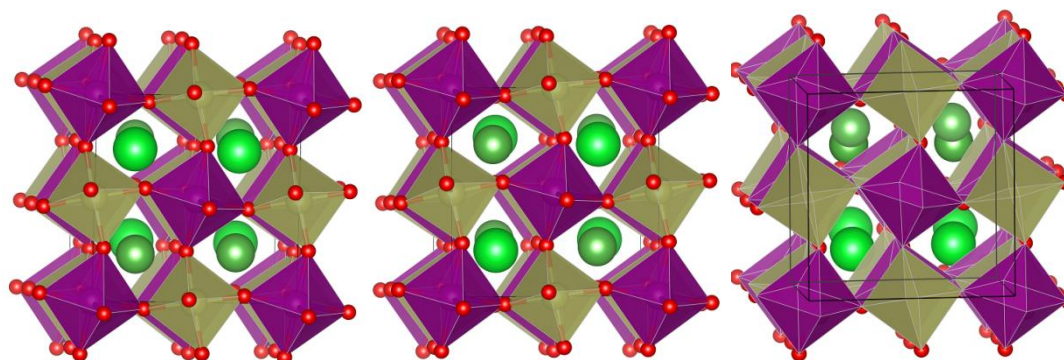


Figure S4. Different A-cations configurations of LSMIO composite considered in this study. (left) columnar type (middle) rocksalt type (right) layer type.

Table S1. Relative energies (meV/f.u.) obtained by GGA scheme within the magnetic ground state, i.e. ferrimagnetic ordering. The results suggest that the columnar type A-cations pattern is preferable in LSMIO composite films.

	Columnar	Rocksalt	Layer
Energy (meV)	0.0	15.7	86.7

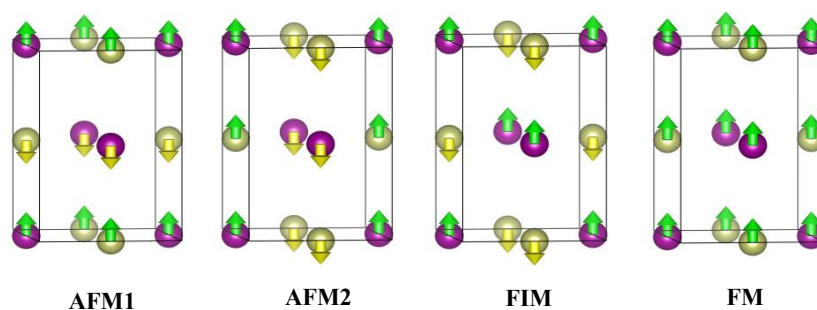


Figure S5. Different magnetic configurations of LSMIO composite considered in this study. Only Mn atoms (purple spheres) and the Ir atoms (brown ones) are shown for simplify. Green (yellow) arrows indicate spin up (down) character.

Table S2. The calculated total energies (eV/2×2×2 supercell) obtained by GGA and GGA+U ($U_{\text{Mn}} = 4.0$ eV, $U_{\text{Ir}} = 2.0$ eV) methods. The FIM (ferrimagnetic) is the ground state.

		FM	FIM	AFM1	AFM2
Energy (eV)	GGA	-302.0302	-302.0391	-301.9835	-301.9835
	GGA+U	-286.4180	-286.9023	-286.2655	-286.5611

We performed electronic calculations on four distinct magnetic alignments: ferromagnetic (FM), ferrimagnetic (FIM) (i.e., with Mn ions being antiferromagnetic (AFM) coupled to six neighboring Ir ions and vice versa) and two distinct AFM ones, within the normal GGA/GGA+U ($U_{\text{Mn}} = 4.0$ eV, $U_{\text{Ir}} = 2.0$ eV) prescriptions with the goal of identifying the magnetic ground state. From the total energy results of the distinct magnetic solutions, we found that the ferrimagnetic, uncompensated antiferromagnetic alignment, due to the unequal magnetic moments on Mn and Ir sites, is the most stable state for LSMIO, irrespective of whether the Hubbard U values was taken into account or not, affirming the experimental magnetic observations.

The conspicuous feature of electronic structure is that most of majority channel of Mn 3d orbitals are occupied, forming a broad valence band ranged from -7.0 eV to the Fermi level, while the corresponding minority channel is entirely empty centered at 4.5 eV above the Fermi level, revealing that electronic configuration is close to the $t_{2g}^{3\uparrow}e_g^{1\uparrow}$ state and the oxidation state is 3+. Unexpected, the magnetic moment at Mn sites is slightly larger than the ideal spin-only $4 \mu_B$ for Mn^{3+} cations, suggesting the special magnetic coupling mechanism behind. For the Ir states, on one hand, the occupied minority Os t_{2g} states are completely separated from the empty e_g states by an energy interval of ~ 4 eV, accompanied by a moderate spin splitting of ~ 2 eV. On the other hand, the spin up t_{2g} states are partially filled, splitting into a small band gap under the Hubbard U correlation effect. As a consequence, electronic configuration is close to the nominal $t_{2g}^{3\downarrow 1\uparrow}$ state and the oxidation state is 5+. In addition, there are some Ir e_g orbitals present around -6 eV below the Fermi level drowned in the O $2p$ manifold, unfolding the strong covalency between the Ir $5d$ and O $2p$ states. The covalent bonding is so strong that the computed Ir magnetic moment ($\sim 0.9 \mu_B$) is remarkable smaller than the ideal spin-only value ($\sim 2 \mu_B$).

The antiferromagnetic coupling and unexpected large magnetic moment on Mn^{3+} site can be interpreted in the framework of superexchange interactions through the virtual hopping bridged by O $2p$ spin-up electrons. We can see that in contrast to the large energy separation of more than 5 eV between the down-spin Mn^{3+} and Ir^{5+} t_{2g} states, the up-spin Mn^{3+} e_g and Ir^{5+} t_{2g} states are separated by on the small band gap of 0.2 eV, and their hybridization via O $2p$ up-spin orbitals can push the occupied Mn^{3+} $t_{2g}^{3\uparrow}e_g^{1\uparrow}$ and Ir^{5+} $t_{2g}^{3\downarrow 1\uparrow}$ bands downwards, consequently stabilizes the antiferromagnetic interaction and then the ferrimagnetic ground state. In other words, the virtual hopping from Ir^{5+} t_{2g}^{\uparrow} to the empty Mn^{3+} e_g^{\uparrow} via the bridged O $2p^{\uparrow}$ states accounts for the antiferromagnetic coupling and the abnormal large computed Mn^{3+} magnetic moment as well as the exclusively negative sign of the induced O^{2-} magnetic moments.